AGU PUBLICATIONS

JGR

Journal of Geophysical Research: Solid Earth

RESEARCH ARTICLE
10.1002/2017JB014935

Key Points:
- Fault orientation of moderate to small earthquakes can be resolved from azimuthal variation in the shape of the whole source time function
- Seven of eight aftershocks (*M* 3–4.5) are predominantly unilateral with rupture direction consistent with the fault plane of the main shock
- Rupture velocity estimates should be considered minima and do not correlate with robust spatial variation in stress drop

Supporting Information:
- Supporting Information S1

Correspondence to:
R. E. Abercrombie,
rea@bu.edu

Citation:
Abercrombie, R. E., Poli, P., & Bannister, S. (2017). Earthquake directivity, orientation, and stress drop within the subducting plate at the Hikurangi margin, New Zealand. *Journal of Geophysical Research: Solid Earth*, *122*, 10,176–10,188. https://doi.org/10.1002/2017JB014935

Received 6 SEP 2017
Accepted 22 NOV 2017
Accepted article online 30 NOV 2017
Published online 13 DEC 2017

Earthquake Directivity, Orientation, and Stress Drop Within the Subducting Plate at the Hikurangi Margin, New Zealand

Rachel E. Abercrombie[1], Piero Poli[2], and Stephen Bannister[3]

[1]Department of Earth and Environment, Boston University, Boston, MA, USA, [2]Department of Earth, Atmospheric and Planetary Sciences, MIT, Cambridge, MA, USA, [3]GNS Science, Lower Hutt, New Zealand

Abstract We develop an approach to calculate earthquake source directivity and rupture velocity for small earthquakes, using the whole source time function rather than just an estimate of the duration. We apply the method to an aftershock sequence within the subducting plate beneath North Island, New Zealand, and investigate its resolution. We use closely located, highly correlated empirical Green's function (EGF) events to obtain source time functions (STFs) for this well-recorded sequence. We stack the STFs from multiple EGFs at each station, to improve the stability of the STFs. Eleven earthquakes (*M* 3.3–4.5) have sufficient azimuthal coverage, and both *P* and *S* STFs, to investigate directivity. The time axis of each STF in turn is stretched to find the maximum correlation between all pairs of stations. We then invert for the orientation and rupture velocity of both unilateral and bilateral line sources that best match the observations. We determine whether they are distinguishable and investigate the effects of limited frequency bandwidth. Rupture orientations are resolvable for eight earthquakes, seven of which are predominantly unilateral, and all are consistent with rupture on planes similar to the main shock fault plane. Purely unilateral rupture is rarely distinguishable from asymmetric bilateral rupture, despite a good station distribution. Synthetic testing shows that rupture velocity is the least well-resolved parameter; estimates decrease with loss of high-frequency energy, and measurements are best considered minimum values. We see no correlation between rupture velocity and stress drop, and spatial stress drop variation cannot be explained as an artifact of varying rupture velocity.

1. Introduction

Earthquake rupture along a fault, or directivity, produces azimuthal variation in the seismic radiation. This directivity can be used to infer both the orientation of the fault plane and the rupture velocity; it also controls the peak ground shaking and damage (e.g., Kanamori et al., 1992). As data quantity and quality have improved, directivity has been observed for moderate-sized (e.g., Boatwright, 2007; McGuire, 2004; Seekins & Boatwright, 2010) and smaller (e.g., Chen, Jordan, & Zhao, 2010; Folesky et al., 2016; Tomic, Abercrombie, & Do, 2009; Yamada et al., 2005) earthquakes. These studies found that most earthquakes with resolvable directivity are predominantly unilateral, and the range of rupture velocities is similar to that of larger earthquakes. Measurements of rupture velocity are important for studies of earthquake scaling, because estimates of stress drop assume a rupture velocity. Even for relatively simple models, variations in symmetry and rupture velocity can lead to a significant variation in stress drop ($\Delta\sigma$) estimate (Kaneko & Shearer, 2015):

$$\Delta\sigma = kcf_c^3 \sim \frac{kc}{T^3} \tag{1}$$

where c is the velocity of the *P* or *S* wave, f_c is the spectral corner frequency, T is the source duration, and k is a constant that decreases with increasing rupture velocity, and an average value is typically assumed. It is possible that short-duration small earthquakes that are interpreted as being high stress drop could simply have high rupture velocities. Causse and Song (2015) proposed that rupture velocity and stress drop are anticorrelated to explain the discrepancy between relative variability of stress drop and peak ground acceleration (Cotton, Archuleta, & Causse, 2013).

Lengliné and Got (2011), Kane et al. (2013), and Wang, Rubin, and Ampuero (2014) used azimuthal variation in spectral amplitudes to infer that the predominant rupture direction of earthquakes on the San Andreas Fault at Parkfield is consistent with the material contrast across the fault. Folesky et al. (2016)

found that rupture direction within a cluster of fluid-induced earthquakes depends on location and magnitude. There is still considerable uncertainty in the results of directivity studies due to lack of resolution of the data. López-Comino et al. (2012) and Park and Ishii (2015) showed how even with good station coverage, pure unilateral rupture cannot often be resolved from asymmetric bilateral rupture. The rupture velocity is more affected by geometric and frequency-bandwidth constraints than the orientation and must usually be considered a minimum due to the limitations of resolution; typically, only the horizontal component of the velocity is considered (e.g., Folesky et al., 2016; López-Comino et al., 2012; Tomic et al., 2009).

To investigate directivity of smaller earthquakes, first, it is necessary to deconvolve the source process from the site and path effects in the recorded seismograms. This is required to prevent azimuthal variations in attenuation being interpreted as source directivity. This potential for misinterpretation is exacerbated by the fact that the orientation of both active faults and anisotropy in attenuation are controlled by tectonic structures. Most studies use a co-located small earthquake as an empirical Green's function (EGF) to do this (e.g., Kanamori et al., 1992; Tomic et al., 2009; Folesky et al., 2016; Wang et al., 2014) but Pacor et al. (2016) used more generalized inversion. Abercrombie (2015) discussed some of the inherent uncertainties in the EGF approach.

The most common method of estimating directivity of smaller earthquakes is to measure the duration of the source pulse (or source time function, STF) at each station and then model to find the best fitting line source (e.g., Tomic et al., 2009; Folesky et al., 2016). Picking the start and end times of pulses is not always straightforward, and some authors for this reason have preferred to model azimuthal variation in amplitude (Pacor et al., 2016). Warren and Silver (2006) developed a "stretching" approach to distinguish between the two nodal planes of large deep-focus earthquakes. They varied the time scale of the *P* waveform recorded at each station and compared it to the other stations, finding the relative stretching that gave the best cross correlation for each pair of stations. They modeled this azimuthal variation to determine which nodal plane was the fault plane. Warren et al. (2015) found that most large deep earthquakes slip on a dominant fault orientation consistent with the slab geometry. Prieto et al. (2017) extended this "stretching" approach to a smaller, unusual deep earthquake beneath Wyoming. They applied the approach to source time functions derived from using EGFs; they varied the time scale of the STF at each station and compared it to the other stations, finding the relative stretching that gave the best cross correlation for each pair of stations. The line source that best matched both *P* and *S* waves was consistent with the NW striking plane of the strike-slip focal mechanism and a relatively low rupture velocity ($0.3 \times V_S$, shear wave velocity). We further develop this stretching approach and apply it to earthquakes within the subducting plate beneath New Zealand. These earthquakes, aftershocks of the 2014 Eketahuna earthquake, were previously analyzed by Abercrombie et al. (2017), who relocated the sequence and calculated STFs and stress drops.

We start by investigating the robustness of the spatial variation in stress drop for earthquakes within the sequence. We then describe the stretching approach and its results and use a number of tests to demonstrate its resolution and uncertainties. We find that directivity orientation is significantly better resolved than rupture velocity. Most of the aftershocks exhibit predominantly unilateral rupture, probably on a plane similar to the main shock fault plane. Variation in stress drop cannot be simply explained by variations in source geometry or rupture velocity.

2. Eketahuna Earthquake Sequence and Data

In January 2014 a M_L 6.2, normal-faulting, earthquake occurred in the subducted Pacific plate beneath Eketahuna, with shaking felt throughout New Zealand. The earthquake was likely associated with deeper slow slip on the subduction interface (Wallace et al., 2014). The Eketahuna earthquake was followed by an extensive aftershock sequence within the thickened crust of the subducting plate (Davy, Hornle, & Werner, 2008). The aftershocks align with the more westerly dipping nodal plane of the main shock, suggesting that it is the fault plane (Figure 1). Regional moment tensors are not available for the aftershocks so we do not know their nodal planes; Abercrombie et al. (2017) could only calculate scalar moments for the largest two events using the GeoNet software.

The Eketahuna earthquake and its aftershocks were well-recorded by the GeoNet national (broadband, 100 samples/s) and regional (short period, 100 samples/s) seismometer networks (Gale et al., 2014) (see

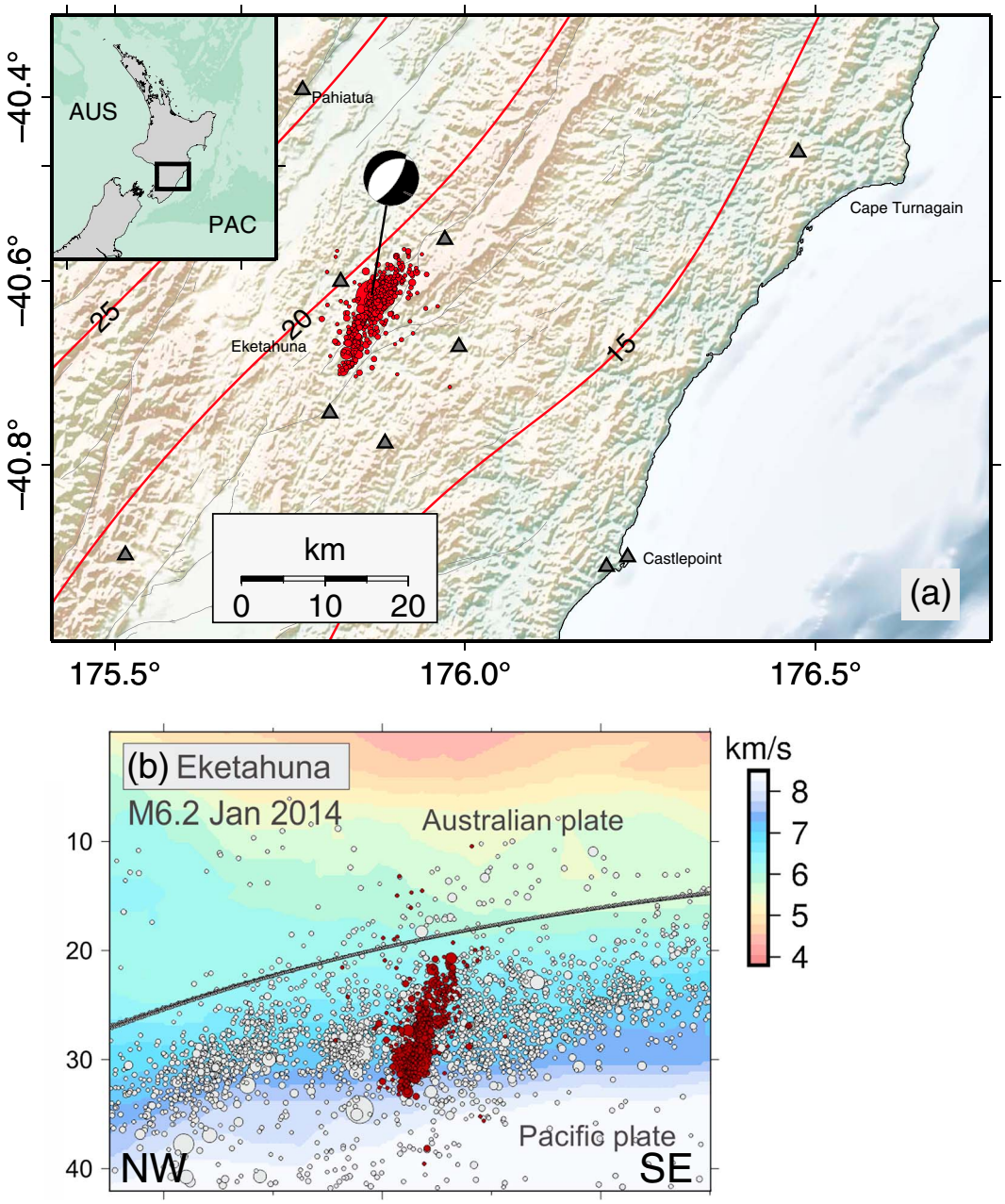

Figure 1. (a) Epicenters of the Eketahuna earthquake sequence, lower North Island, New Zealand (red circles); the inset shows the map location within New Zealand. The main shock focal mechanism was derived by moment tensor inversion (http://www.geonet.org.nz; last accessed 29 August 2017), plotted with upper hemisphere projection. GeoNet seismometer site locations are shown as triangles. The contours with dashed red lines show the depth to the subduction interface, as derived by Williams et al. (2013). (b) NW-SE cross section through the earthquake sequence. The white open circles show background seismicity for years 2001–2011 for earthquakes within 40 km of the cross section; the red circles show the projection of the aftershock sequence hypocenters. The gray line shows the depth of the subduction interface estimated by Williams et al. (2013). *P* wave velocity (km/s) is shown in the background, from the 3-D New Zealand velocity model of Eberhart-Phillips et al. (2010).

Data and Resources). This sequence was included in the stress drop analysis of Abercrombie et al. (2017). Earthquake locations in New Zealand are routinely determined by GeoNet (www.geonet.org.nz) using the 3-D velocity model of Eberhart-Phillips et al. (2010). Abercrombie et al. (2017) relocated the aftershocks using double-difference relocation (Waldhauser & Ellsworth, 2000), including waveform-based differential times calculated for all event-station pairs using ObsPy (Beyreuther et al., 2010).

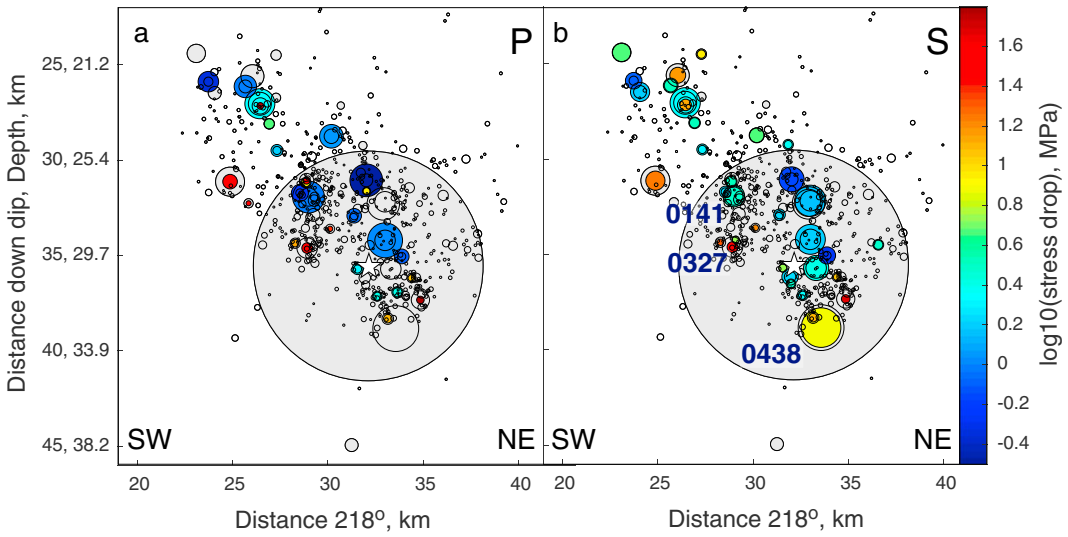

Figure 2. Spatial distribution of stress drop projected onto the main shock fault plane. All relocated aftershocks are plotted as open circles, and the gray circles are the 50 events analyzed by Abercrombie et al. (2017), sized to the radius for a stress drop of 5 MPa (median value). (a) The colored circles are *P* wave stress drop results, using cross correlation of at least 0.75. (b) Same as in Figure 2a but for *S* wave stress drop results.

3. EGF Analysis and Calculation of Source Time Functions

We use the source time functions determined using the EGF analysis described by Abercrombie et al. (2017). In their study, only the average spectral ratios and STFs per event were used, stacked over all stations. Here we focus on the best-recorded earthquakes for which stacked STFs can be calculated at sufficient individual stations to identify azimuthal variation (Table S1 in the supporting information).

The full details of the EGF analysis are given in Abercrombie et al. (2017), and we summarize the main points here. The approach focuses on including only highly appropriate EGFs, identified by both proximity and cross correlation.

For each target earthquake, in turn, we identify potential EGF events from the catalogues, following the approach of Abercrombie (2013, 2014, 2015). We include all earthquakes within 2 km epicentral distance of the target earthquake (larger than the location uncertainty) and between 1 and 2.5 magnitude unit smaller. We calculate a window length (ns) that is of the order of 10 times the expected pulse duration of the target earthquake using

$$\mathrm{ns} = \mathrm{round}\left(10 \times M_0^{1/3}/20,000\right)/10 \tag{2}$$

where M_0 is the seismic moment of the target earthquake, in Nm. This window length is used for both *P* and *S* waves for the target earthquake and all EGFs. We then cross-correlate each EGF with the target event, for *P* and *S* waves, at all stations, after applying a low-pass filter to both the target earthquake and each potential EGF at a frequency related to the expected corner frequency of the target event, assuming constant stress drop (10/ns). Large and small earthquakes are not expected to cross-correlate well at high frequencies.

We use a default high-pass corner of 0.5 Hz to remove microseismic noise (large in New Zealand). If the pair of seismograms (target and EGF) has a cross correlation of ≥0.7, we calculate their spectra, spectral ratios, and the relative source time functions (STFs) using the multitaper method of Prieto, Parker, and Vernon (2009) and the unfiltered seismograms. We then stack (by calculating the mean) the resulting spectral ratios and STFs by event and also by EGF and by station. Each stack contains at least 5 ratios or STFs. Stacking the results from multiple EGFs cancels out any complexity or directivity in an individual EGF, meaning that any observed complexity or azimuthal variation must be a feature of the target earthquake (e.g., Calderoni et al., 2015; Ross & Ben-Zion, 2016).

For the Eketahuna sequence, Abercrombie et al. (2017) started with 674 earthquakes $M_L \geq 2$ and were able to calculate source parameters for 46 of the 50 earthquakes with $M_L \geq 3.2$. Figure 2 shows the spatial variation of

stress drop calculated by Abercrombie et al. (2017) for the sequence, assuming the models of Eshelby (1957), Boatwright (1980), and Kaneko and Shearer (2015). They were unable to get good results for the main shock due to the lack of EGFs, but strong motion modeling suggests a relatively simple source, probably smaller than the gray circle plotted (Van Houtte et al., 2017). The location of the main slip is unknown with respect to the aftershocks but probably occurred in the region of few aftershocks downdip and to the SW of the hypocenter (Ross, Kanamori, & Hauksson, 2017). It is unknown whether the aftershocks mainly occurred on the main shock fault plane. Figure 2 shows coherent spatial variation that is consistent between the independent *P* and *S* wave measurements, suggesting that it is real. All measurements are made using highly correlated EGFs, and the variation is larger than the calculated uncertainties that include spectral misfit and interstation variability (Table S1). These measurements all assume a simple circular source and that the rupture velocity is a constant fraction of 0.7 of the depth-corrected shear wave velocity (constant *k*, equation (1)). It is possible that these apparent variations in stress drop are an artifact of rupture velocity differences causing the variation in source duration. Alternatively, Causse and Song (2015) suggested that rupture velocity and stress drop could be anticorrelated, in which case the stress drop variations would be larger than those calculated assuming a constant rupture velocity.

4. Stretching and Modeling STFs

Eleven (*M* 3.3–4.5) of the earthquakes analyzed by Abercrombie et al. (2017) have stacked STFs at sufficient stations, with good enough azimuthal distribution to attempt to resolve directivity. The total number of stations per event ranged from 16 (minimum *P* = 4, minimum S = 10) to 45, with a median of 34. Hypocentral and source parameter information for these earthquakes are included in Table S1.

4.1. Stretching Method

First we band-pass filter the STFs between 2/ns and a maximum frequency of 40 Hz for *P* waves and 25 Hz for *S* waves based on the signal-to-noise criteria calculated by Abercrombie et al. (2017). Using a constant maximum frequency means that the smaller and shorter duration earthquakes are relatively more filtered.

The rupture duration (T) at station i given a line source of size L is given by

$$T_i = L/Vr(1 - \cos\theta_i \sin\phi_i \sin\delta Vr/V - \cos\phi_i \cos\delta Vr/V) \quad (3)$$

where Vr is the rupture velocity, V is the P (V_P) or S (V_S) wave velocity at the source, ϕ_i is the takeoff angle, and θ_i and δ are the azimuth and dip of the rupture direction, respectively (dip is defined as 0 = vertically up, 90 = horizontal, and 180 = vertically down). The takeoff angles are calculated using ray tracing in the local velocity model, for the relocated sources (Abercrombie et al., 2017).

From equation (3) we define the stretching S_{ij} between two stations as

$$S_{ij} = T_i/T_j \quad (4)$$

The stretching in equation (4) is measured in between each pair of stations, by fixing the length of one STF, while time resampling the second one. For each time resampling (stretching or compressing) the correlation between two STFs is calculated, and the preferred S_{ij} is the one with the maximum correlation coefficient. Only S_{ij} with a correlation coefficient larger than 0.9 are retained for further analysis. We also ensure that the ratio $\frac{S_{ji}}{S_{ij}} \sim 1$. We thus have a set of robust stretching values, from which we can obtain the rupture angles and rupture velocity (substituting equation (3) into equation (4)) by grid searching over all possible combinations. The source size L cancels out in equation (4) because, unlike the other parameters, it does not affect the relative variation in duration between stations or phases. To estimate L, we would need to measure the actual duration (T_i) at a reference station, and then solve equation (3) using the best fitting model from the inversion of the stretching values.

The inversion of the stretching values minimizes the L1 norm for *P* and *S* waves separately and combined. For each earthquake, we invert for three simple line source types: a purely unilateral, a symmetric bilateral, and an intermediate, asymmetric bilateral rupture propagating for twice the distance in one direction and as in the other opposite one. We determine whether these end-member models are distinguishable by comparing the misfit of the final solution to the data; the preferred final solution is chosen as the one with the lowest misfit.

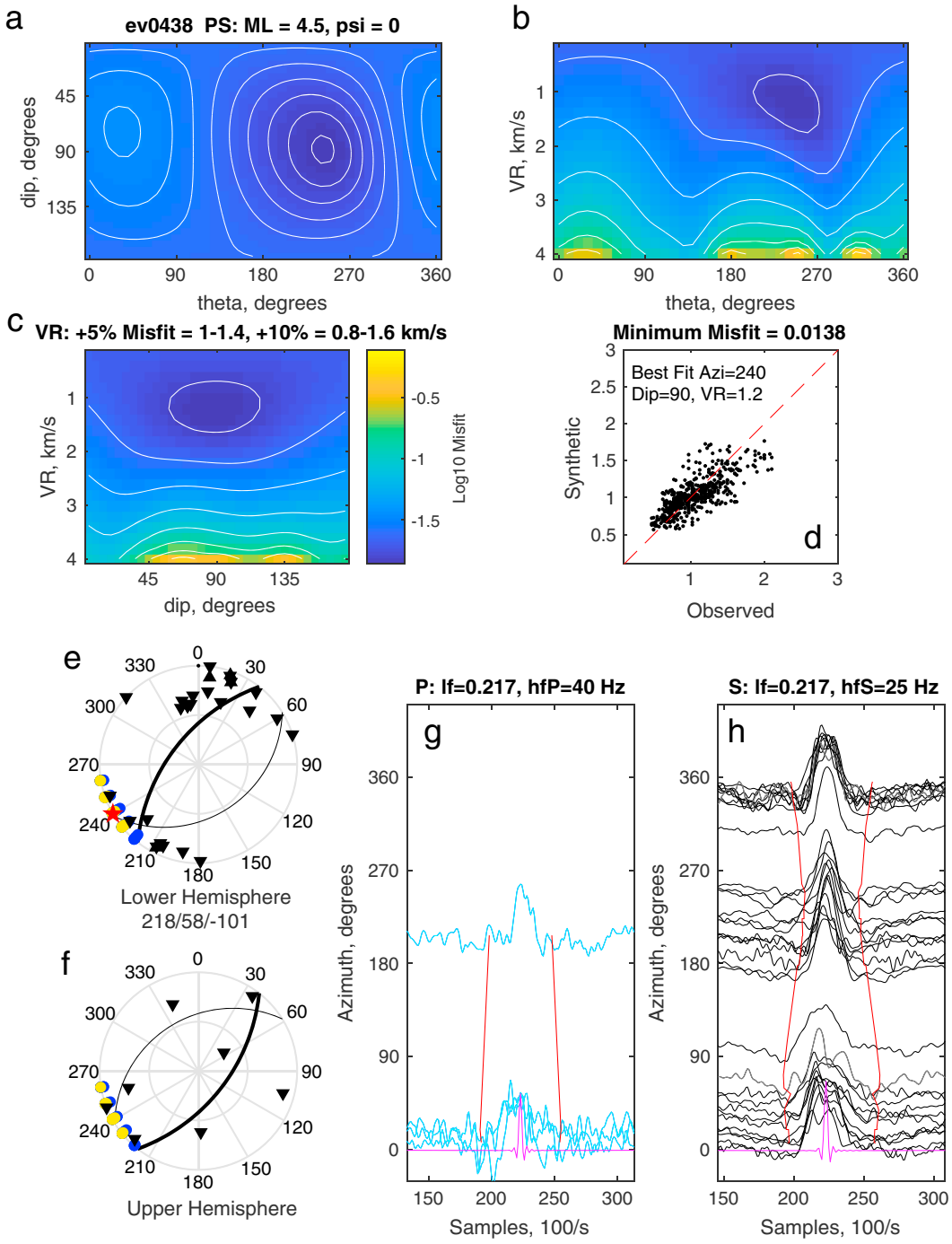

Figure 3. Example of unilateral directivity modeling for earthquake 0438, *M* 4.5. (a–c) The three color contour maps show the misfit between the azimuthal variation in stretching of the STFs and the unilateral line source, as a function of line azimuth (theta), dip (0 = vertically up, 90 = horizontal, and 180 = vertically down), and rupture velocity. (d) The scatterplot shows the relative stretching between each pair of stations from the STFs compared to that predicted by the best fitting line source. The red line shows 1:1 correspondence. (bottom left) The (e) lower and the (f) upper hemisphere focal spheres; the main shock focal mechanism (strike/dip/rake) is plotted on both (fault plane thicker line), but otherwise, they only show upper and lower hemisphere angles, respectively. The black triangles are the stations used (upward point for *P*, downward for *S*, and superimposing as a star if both *P* and *S*), the red star is the best fitting line source (minimum misfit), the yellow region shows the directions with misfit within 5% of the minimum, and the blue the directions within 10% of the minimum. (bottom right) The (g) *P* wave (blue, cyan if not included) and the (h) *S* wave (black, gray if not included) source time functions used in the analysis. The filter frequencies are given. The red lines indicate how the duration varies for the best fitting line source. They are centered on the STFs and have a mean duration corresponding to the approximate duration of the STF obtained by stacking all stations together. The magenta STF is the resolved delta function—the result of deconvolving the main event from itself. A similar plot showing the best fit with a bilateral model is shown in Figure S2.

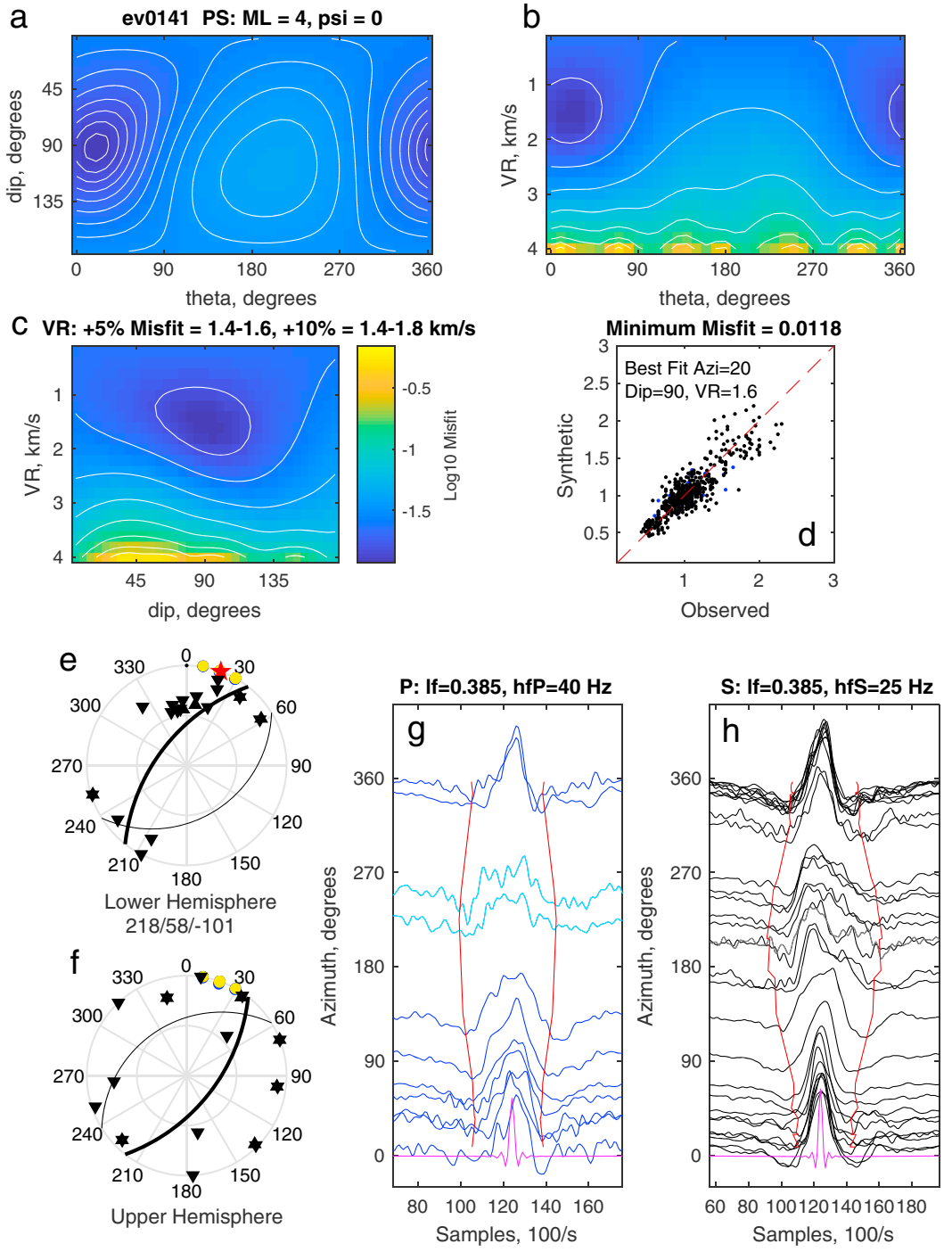

Figure 4. Example of unilateral directivity modeling for earthquake 0141, *M* 4.0. See Figure 3 for details. A similar plot showing the best fit with a bilateral model is shown in Figure S2.

4.2. Results of Stretching

The results of the stretching and fitting are shown in Figures 3 and 4 and S1 and S2 in the supporting information. Of the 11 earthquakes considered, 8 have sufficient azimuthal variation to place reliable constraints on the orientation and velocity of the rupture (Figure 5 and Table S2). A unilateral line source is a better fit than the bilateral one to all but one event (0468). The difference between unilateral and bilateral fits can be significant, for example, for earthquake 0141, but for other earthquakes, it is more marginal. For

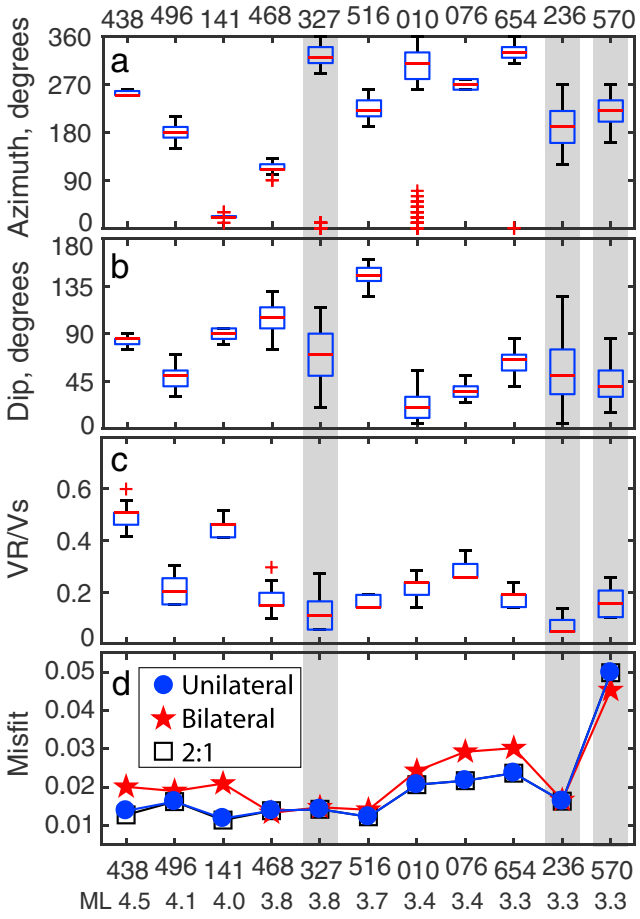

Figure 5. Results of directivity modeling. (a–c) Box-and-whisker plots (the red crosses are outliers) of the grid search results for the 2:1 asymmetrical bilateral model (identical to the unilateral model for all events except 0438 and 0141), within 5% of the minimum misfit for *P* and *S* waves combined. The velocities are divided by the depth-corrected shear wave velocity. The depth correction is small; V_S increases by less than 10% from 3.9 to 4.3 km/s over the depth range. (d) Minimum misfits from the three different models. For most earthquakes the bilateral model has a higher misfit than the unilateral. The gray shading highlights the three events with poor resolution and poor fits for all source models. The 2:1 asymmetric bilateral model is either almost or completely indistinguishable from the unilateral model.

all but two earthquakes (0141 and 0438) the 2:1 asymmetrical bilateral rupture resulted in exactly the same orientation, rupture velocity, and misfit as the unilateral model (Figures 5 and S3). For these two earthquakes the asymmetrical model has slightly lower misfit and negligible difference in orientation but higher rupture velocity (1.8 km/s compared to 1.6 km/s for 0141 and 2.0 km/s compared to 1.2 km/s for earthquake 0438). Depending on the rupture geometry and rupture velocity it can be impossible to distinguish between completely unilateral and only partly asymmetric sources even with good azimuthal distribution of stations (e.g., López-Comino et al., 2012; Park & Ishii, 2015).

The rupture directions of all of the resolvable earthquakes are consistent with them occurring on the NW dipping main shock fault plane. Four of the earthquakes (0010, 0076, 0141, and 0654) prefer the main shock plane, and the other four have directions too close to the null axis to distinguish between the planes. These results are consistent with those of Warren et al. (2015) for deeper earthquakes, who found a predominant orientation for intraslab events.

The rupture velocities that we obtain for the best-fitting unilateral models are relatively low, mostly below 50% of the shear wave velocity. These are low even for minimum values and, allowing asymmetric bilateral rupture, only has a significant effect for the largest earthquake. It is possible that these intraslab earthquakes have low rupture velocities, in which case all the calculated stress drops would be underestimates.

Alternatively, it could be that rupture velocity is poorly resolved in the present analysis. The three earthquakes for which we could not resolve directivity had, on average, the shortest durations. The frequency bandwidth-limited data mean that we could be overestimating the source pulse at some azimuths (e.g., Tomic et al., 2009). When we invert the *P* and *S* waves separately we find consistently higher rupture velocities for the *P* than for the *S* waves, for the few events with sufficient *P* wave STFs to constrain a solution. This disparity can be understood by considering the implications of equation (3) for local and regional recording. For a horizontal rupture, station regional distances will record a much greater variation in apparent rupture duration than those directly above, or at teleseismic distances. For a horizontally propagating, unilateral rupture the difference between maximum and minimum pulse durations recorded by stations at 90 takeoff angles becomes $1 \pm Vr/V$. Hence, for a rupture velocity of $0.9V_S$, and $V_P/V_S = 1.73$, the range of pulse durations is a factor of 3 for *P* waves and 19 for *S* waves. The signal bandwidth of *S* waves for small earthquakes is rarely large enough to resolve such a range of pulse durations without distortion and filtering. These would decrease the apparent range of pulse durations and hence the apparent rupture velocity calculated. The *S* waves clearly provide significant information about the rupture orientation and so we prefer not to eliminate them. We tried various different inversion weighting schemes and two stage inversions in an attempt to use the *S* waves to constrain the orientation and the *P* waves, the rupture velocity. We even considered joint inversions where the rupture velocity used for the *S* waves was lower than that for the *P* waves. We could obtain better fits for some events in this manner, but the increased complexity required too many subjective choices of inversion input parameters to be robust. The main conclusion from these attempts was that the orientations are relatively stable and that the limited bandwidth of the *S* wave STFs is artificially lowering the rupture velocity results.

To investigate the resolution of our stretching method for both rupture velocity and orientation more objectively, we vary the filtering and perform some synthetic tests.

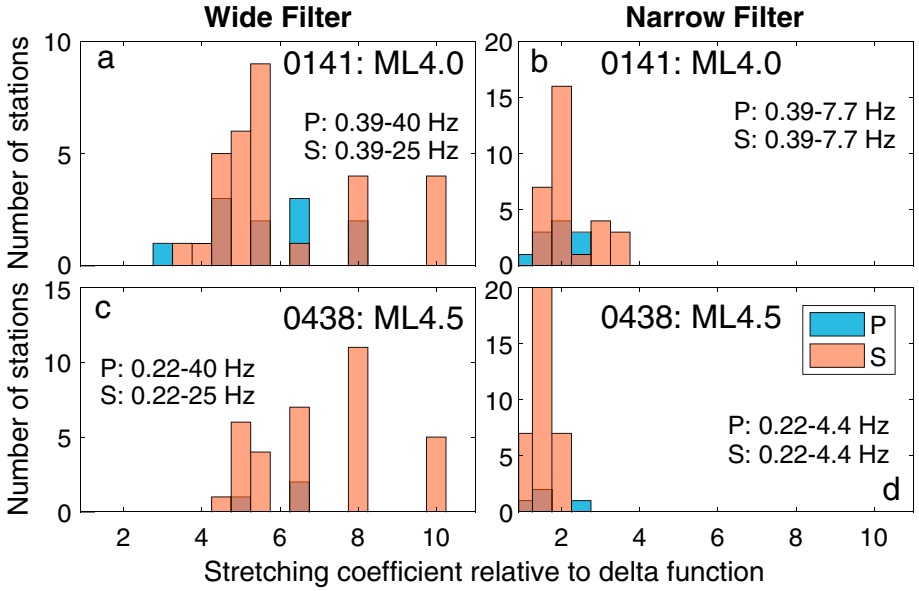

Figure 6. Duration of the observed STFs to the resolvable delta function. Histograms for the stretching coefficient of both *P* and *S* waves, to their respective resolvable delta functions, for earthquake 0141 using (a) the wide filter and (b) the narrow filter. (c and d) The same for earthquake 0438. The wide filter is that used in the preceding analysis, and the narrower is the magnitude-dependent filter.

5. Resolution Tests

We perform two different tests to investigate the resolution of our approach and results. First we calculate the resolved "delta function" by deconvolving the target event from itself; the resulting STF is how a real input delta function would be resolved in our data. We then repeat the stretching analysis with respect to this resolved delta function, for two different high-pass filters. Second, we stretch the resolved delta function as expected for different rupture velocities to calculate synthetic STFs. We repeat the stretching analysis, following filtering, to determine what we can resolve.

5.1. Resolvable Delta Function

If the pulse duration at any azimuths is shorter than the minimum resolvable pulse, then it will affect the modeling of azimuthal variation (e.g., Tomic et al., 2009). We use each seismogram as an EGF of itself and therefore calculate the resolvable delta functions. Since we use the same filters and sample rates for all stations, there is only one value for each of the *P* and *S* waves per event. They are plotted in Figures 3 and 4 and S1 and S2, for comparison with the deconvolved STFs. For the largest events, the resolved delta functions are significantly shorter than all the STFs, but this is decreasingly true for the smaller earthquakes and those with shorter average durations (e.g., 0327 and 0236). To quantify the effects of this resolution issue, for each earthquake, we calculate the relative stretching of each STF to the resolvable delta function for the earthquake. We then repeat the analysis after applying a smaller, magnitude-dependent frequency bandwidth (2/ns to 40/ns Hz) filter to the STFs and the delta functions, to investigate how resolution may be lost for smaller earthquakes. Figure 6 shows that variation in STF durations is less for the narrower frequency range and for smaller earthquakes. The lower the maximum frequency, the longer the resolvable delta function. The two best resolved earthquakes (0141 and 0438) have much larger variation in *S* wave STFs than in *P*, as expected.

We repeated the entire original stretching analysis after applying the narrower filters to the STFs. The filtered STFs are simpler and cross-correlate better (compare Figure S6 to Figures 3, 4, and S1) so the approach works well. The resolvable delta functions are significantly longer. The resulting rupture directivity orientations vary relatively little, but the rupture velocities decrease by about 20% for even the two best resolved events.

5.2. Modeling Synthetic STFs for Varying Rupture Velocities

To quantify the effect of signal frequency range on the resolution we perform a synthetic test. We use equation (2) to calculate the stretching coefficients for a unilateral rupture propagating horizontally due north at a

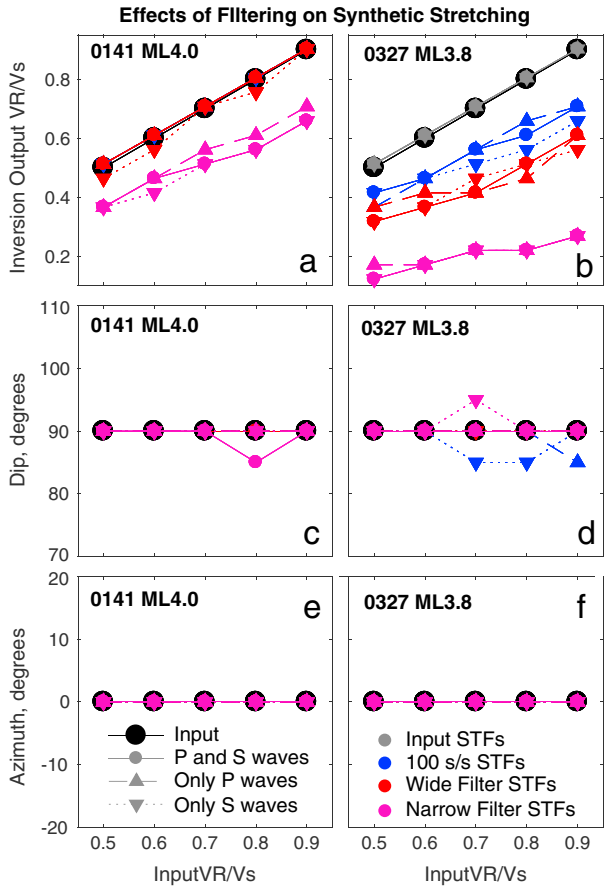

Figure 7. Synthetic tests of resolution. For earthquake (a, c, and e) 0141 and (b, d, and f) 0327 we show how well the input orientation and rupture velocity parameters are recovered, for *P* and *S* waves separately and combined, for different input velocities. The large black circles are the input values. The triangles and inverted triangles are the results of inversion of *P* and *S*, respectively and the circles are for combined *P* and *S*. The colors represent different sampling rates and filtering applied to the synthetic STFs before inversion. The orientation (Figures 7c–7f) is very stable, independent of rupture velocity and filtering. The rupture velocity is underestimated for the narrow filtering for earthquake 0141 (Figure 7a), and for decimation and all filtering options for the shorter input pulses of the smaller earthquake 0327 (Figure 7b).

range of rupture velocities, for the station distribution that recorded earthquake 0141. We divide the stretching coefficients by two and apply them to the average STF (stack over all stations) for this event to calculate realistic STFs corresponding to the input model. We divide by two to half the duration of all synthetic STFs in case the average is an over estimate (i.e., some STFs are not much longer than the resolvable delta function). Since for higher rupture velocities, short pulses are calculated, we increase the sampling rate by a factor of four before stretching to obtain sufficient resolution of the input synthetics. We then decimate and filter these resulting synthetic STFs to the same sample rate and the same frequency bandwidth that we use to analyze the original data and invert them as for the real data. We repeat this synthetic analysis for a smaller earthquake (0327), with a shorter average duration, for which we could not resolve directivity. To account for our average pulse being an overestimate of this shorter earthquake, we divide all the stretching coefficients by 3.

Figure 7 shows the input values and inversion results for the synthetic tests of both earthquakes. The inversion of the input STFs before decimation or filtering recovers the input values of all model parameters. The orientation of the rupture is remarkably stable for both earthquakes, for all rupture velocities and filters, implying that resolution and frequency limitations are not a major cause of uncertainty in orientation. The recovered rupture velocity is significantly affected by the lower sampling rate and the filtering, especially for the shorter duration earthquake 0327. The *S* waves also produce systematically lower rupture velocities than the *P* waves, consistent with our inversions of the real data. Figure S7 shows how the filtering affects the range of measured stretching coefficients for these synthetic tests.

For earthquake 0141, the inversion of the synthetics produced after applying the wider, original filters is able to recover relatively high rupture velocities. This suggests that the velocities we observe for this earthquake and earthquake 0438 are probably closer to the real values but that those of the smaller earthquakes are increasingly likely to be underestimates. A comparison of the range of stretching coefficients of earthquake 0141 and 0438 for the different filters (Figure 6) suggests that when the overall range of stretching coefficients of regional data with the resolvable delta function is within the range 1–4, then rupture velocity is likely an underestimate.

6. Discussion

Using the stretching approach, combined with EGF deconvolution to isolate the source process, we are able to obtain estimates of rupture orientation and velocity for eight earthquakes in the subducting Hikurangi slab.

We perform tests to quantify the resolution and find that the orientations are better constrained than the rupture velocity, which must usually be considered a minimum estimate. Huang, Aso, and Tsai (2017) applied a similar stretching-based approach to larger earthquakes at longer periods and found that rupture velocity tends to be underestimated, whereas orientation is well-resolved. Our tests demonstrate that the finite bandwidth of the signal is a major contribution to the underestimation of rupture velocity; we would recommend that anyone applying such a method should also perform some simple synthetic testing to investigate the resolution.

Huang et al. (2017) also noted that the stretching methods work better for complex ruptures than does the second-order moment approach (McGuire, 2004). In the case of complex ruptures, with multiple subevents,

rupture velocities calculated using a line source will represent a lower bound, as discussed by Park and Ishii (2015). More detailed modeling is to be preferred, but for many earthquakes of interest, the data are insufficient to resolve more complex sources. Folesky et al. (2016) found that the azimuthal variations in amplitude were less affected by filtering than the duration and so could also resolve orientation and rupture velocity. Their approach requires the same EGFs to be used at each station to preserve relative amplitude, limiting the input data. The effect of filters has not been quantitatively tested on amplitude measurements, and source complexity cannot be resolved using only peak amplitude measurements.

All of these simple modeling approaches ignore the existence of a finite risetime, or slip duration, of the kind proposed by Heaton (1990), and now a standard parameter in finite-fault inversions. If all the observed STFs for an earthquake include such an azimuthally independent risetime, then the observed stretching coefficients would be underestimates, also meaning that the calculated rupture velocity should be considered a minimum.

The application of our method to the Eketahuna earthquake sequence reveals that rupture directions of all the earthquakes are consistent with slip on a plane similar to the inferred main shock fault plane (Figures 2, 3, and S1). We do not observe a preferred rupture direction, nor is there any evidence of strong differences in rheology across the fault plane. Warren et al. (2015) found that the orientation of active faults at intermediate depths within subducting plates is controlled by the geometry of the subduction. Our results imply that the smaller aftershocks, as well as the larger main shocks, occur on the same, or similarly oriented, structures.

In more general terms, the lack of resolution does not allow us to resolve any clear variation of rupture velocity with depth or magnitude. We also do not observe any clear relationship between the stress drops obtained in the earlier study and the rupture directions or rupture velocities. The earthquakes with the highest stress drops have the shortest pulses with the least azimuthal variation and so any directivity is least well resolved. In the stress drop analysis, a rupture velocity of 70% of the shear wave velocity was assumed (Abercrombie et al., 2017; Kaneko & Shearer, 2015). If the rupture velocities really were significantly lower, then the corresponding absolute stress drops would be higher because the earthquakes would rupture smaller areas.

Cotton et al. (2013) pointed out the problem of higher variability of earthquake stress drops than peak ground acceleration (PGA), which has significant consequences for seismic hazard analysis (Baltay, Hanks, & Abrahamson, 2017). This could result from the real uncertainties in stress drop being larger than those typically acknowledged, or from other contributing factors, such as variation of rupture velocity. Causse and Song (2015) recently proposed that stress drop and rupture velocity are inversely correlated, to explain observations of PGA variability. At first glance this appears consistent with the present results, but actually, it is somewhat convoluted. In spectral studies, the actual measurement is of the duration (or corner frequency); the stress drop variation comes from the variation in duration measurements (equation (1)). A rupture velocity must be assumed to calculate stress drop from the duration or corner-frequency measurement. If the rupture velocity were lower than assumed, then the duration (or corner-frequency) measurement would imply an even higher stress drop, producing the reverse effect.

Our main observation is that a constant rupture velocity for all the earthquakes studied here is well within the uncertainties, and so the spatial variation in relative stress drop shown in Figure 1 remains likely to be real. It is interesting to speculate on what could cause such strong variation in stress drop over relatively short distances; one possibility is variability in the stress field following the main shock, or alternatively, it could be a consequence of inherent variability in geometry or rheology, for example, in fault roughness (Candela et al., 2011).

7. Conclusions

We present a new approach to calculate rupture orientation, directivity, and velocity for small earthquakes and apply it to an aftershock sequence within the subducting plate at the Hikurangi margin. We find that our combination of the stretching method with high-quality EGFs to isolate the earthquake source is a powerful tool to illuminate the fault plane responsible for the rupture, while minimizing the effects of propagation.

1. By stretching and cross-correlating the source time functions, we use the whole waveform to quantify azimuthal variation; our method does not depend on estimates of the starting, ending, or duration of the source that are often hard to resolve unambiguously.
2. We are able to resolve directivity for 7 out of 11 earthquakes, *M* 3.3–4.5. Of these, six are better fit with unilateral rupture. It is impossible to distinguish pure unilateral rupture from asymmetric bilateral rupture for most events. Hence, the rupture velocities must be considered minimum estimates.
3. Spatial variation in relative stress drop is stable and cannot be explained as a simple trade-off with rupture velocity or rupture orientation.

Acknowledgments
We thank B. Froment for advice and assistance when starting the directivity modeling. We are grateful for the constructive comments by the Editor and two anonymous reviewers which improved this manuscript. The seismic phase data, waveform data, and moment tensor data used in this study were accessed through New Zealand GeoNet (http://www.geonet.org.nz; last accessed 29th August 2017). This research was partially sponsored by the National Science Foundation (USA), Award 1551758, and supported by public research funding from the Government of New Zealand. Maps were drawn using the Generic Mapping Tools (Wessel & Smith, 1998), and some analyses were carried out using ObsPy (Beyreuther et al., 2010).

References

Abercrombie, R. E. (2013). Comparison of direct and coda wave stress drop measurements for the Wells, Nevada, earthquake sequence. *Journal of Geophysical Research: Solid Earth*, *118*, 1458–1470. https://doi.org/10.1029/2012JB009638

Abercrombie, R. E. (2014). Stress drops of repeating earthquakes on the San Andreas Fault at Parkfield. *Geophysical Research Letters*, *41*, 8784–8791. https://doi.org/10.1002/2014GL062079

Abercrombie, R. E. (2015). Investigating uncertainties in empirical Green's function analysis of earthquake source parameters. *Journal of Geophysical Research: Solid Earth*, *120*, 4263–4277. https://doi.org/10.1002/2015JB011984

Abercrombie, R. E., Bannister, S., Ristau, J., & Doser, D. (2017). Variability of earthquake stress drop in a subduction setting, the Hikurangi Margin, New Zealand. *Geophysical Journal International*, *208*(1), 306–320. https://doi.org/10.1093/gji/ggw393

Baltay, A. S., Hanks, T. C., & Abrahamson, N. A. (2017). Uncertainty, variability, and earthquake physics in groundmotion prediction equations. *Bulletin of the Seismological Society of America*, *107*. https://doi.org/10.1785/0120160164

Beyreuther, M., Barsch, R., Krischer, L., Megies, T., Behr, Y., & Wassermann, J. (2010). ObsPy: A Python toolbox for seismology. *Seismological Research Letters*, *81*, 530–533. https://doi.org/10.1885/gssrl.81.3.530

Boatwright, J. (1980). A spectral theory for circular seismic sources: Simple estimates of source dimension, dynamic stress drop, and radiated seismic energy. *Bulletin of the Seismological Society of America*, *70*, 1–28.

Boatwright, J. (2007). The persistence of directivity in small earthquakes. *Bulletin of the Seismological Society of America*, *97*, 1850–1861. https://doi.org/10.1785/0120050228

Calderoni, G., Rovelli, A., Ben-Zion, Y., & Di Giovambattista, R. (2015). Along-strike rupture directivity of earthquakes of the 2009 L'Aquila, central Italy, seismic sequence. *Geophysical Journal International*, *203*(1), 399–415. https://doi.org/10.1093/gji/ggv275

Candela, T., Renard, F., Bouchon, M., Schmittbuhl, J., & Brodsky, E. E. (2011). Stress drop during earthquakes: Effect of fault roughness scaling. *Bulletin of the Seismological Society of America*, *101*, 2369–2387. https://doi.org/10.1785/0120100298

Causse, M., & Song, S. G. (2015). Are stress drop and rupture velocity of earthquakes independent? Insight from observed ground motion variability. *Geophysical Research Letters*, *42*, 7383–7389. https://doi.org/10.1002/2015GL064793

Chen, P., Jordan, T. H., & Zhao, L. (2010). Resolving fault plane ambiguity for small earthquakes. *Geophysical Journal International*, *181*, 493–501. https://doi.org/10.1111/j.1365-246X.2010.04515.x

Cotton, F., Archuleta, R., & Causse, M. (2013). What is the sigma of the stress drop? *Seismological Research Letters*, *84*(1), 42–48. https://doi.org/10.1785/0220120087

Davy, B., Hornle, K., & Werner, R. (2008). Hikurangi Plateau: Crustal structure, rifted formation, and Gondwana subduction history. *Geochemistry, Geophysics, Geosystems*, *9*, Q07004. https://doi.org/10.1029/2007GC001855

Eberhart-Phillips, D., Reyners, M. E., Bannister, S. C., Chadwick, M. P., & Ellis, S. M. (2010). Establishing a versatile 3-D seismic velocity model for New Zealand. *Seismological Research Letters*, *81*, 992–1000. https://doi.org/10.1785/gssrl.81.6.992

Eshelby, J. D. (1957). The determination of the elastic field of an ellipsoidal inclusion and related problems. *Proceedings of the Royal Society of London A*, *241*(1226), 376–396. https://doi.org/10.1098/rspa.1957.0133

Folesky, J., Kummerow, J., Shapiro, S. A., Häring, M., & Asanuma, H. (2016). Rupture directivity of fluid-induced microseismic events: Observations from an enhanced geothermal system. *Journal of Geophysical Research: Solid Earth*, *121*, 8034–8047. https://doi.org/10.1002/2016JB013078

Gale, N., Gledhill, K., Chadwick, M., & Wallace, L. (2014). The Hikurangi margin continuous GNSS and seismograph network of New Zealand. *Seismological Research Letters*, *86*(1), 101–108. https://doi.org/10.1785/0220130181

Heaton, T. H. (1990). Evidence for and implications of self-healing pulses of slip in earthquake rupture. *Physics of the Earth and Planetary Interiors*, *64*(1), 1–20. https://doi.org/10.1016/0031-9201(90)90002-F

Huang, H.-H., Aso, N., & Tsai, V. C. (2017). Toward automated directivity estimates in earthquake moment tensor inversion. *Geophysical Journal International*, *211*(2), 1062–1076. https://doi.org/10.1093/gji/ggx354

Kanamori, H., Thio, H.-K., Dreger, D., & Hauksson, E. (1992). Initial investigation of the Landers, California, earthquake of 28 June 1992 using TERRAscope. *Geophysical Research Letters*, *19*(22), 2267–2270. https://doi.org/10.1029/92GL02320

Kane, D. L., Shearer, P. M., Goertz-Allmann, B. P., & Vernon, F. L. (2013). Rupture directivity of small earthquakes at Parkfield. *Journal of Geophysical Research: Solid Earth*, *118*, 212–221. https://doi.org/10.1029/2012JB009675

Kaneko, Y., & Shearer, P. M. (2015). Variability of seismic source spectra, estimated stress drop and radiated energy, derived from cohesive-zone models of symmetrical and asymmetrical circular and elliptical ruptures. *Journal of Geophysical Research. Solid Earth*, *120*, 1053–1079. https://doi.org/10.1002/2014JB011642

Lengliné, O., & Got, J.-L. (2011). Rupture directivity of micro-earthquake sequences near Parkfield, California. *Geophysical Research Letters*, *38*, L08310. https://doi.org/10.1029/2011GL047303

López-Comino, J.-Á., Mancilla, F., Morales, J., & Stich, D. (2012). Rupture directivity of the 2011, M_w 5.2 Lorca earthquake (Spain). *Geophysical Research Letters*, *39*, L03301. https://doi.org/10.1029/2011GL050498

McGuire, J. (2004). Estimating finite source properties of small earthquake ruptures. *Bulletin of the Seismological Society of America*, *94*(2), 377–393. https://doi.org/10.1785/0120030091

Pacor, F., Gallovič, F., Puglia, R., Luzi, L., & D'Amico, M. (2016). Diminishing high-frequency directivity due to a source effect: Empirical evidence from small earthquakes in the Abruzzo region, Italy. *Geophysical Research Letters*, *43*, 5000–5008. https://doi.org/10.1002/2016GL068546

Park, S., & Ishii, M. (2015). Inversion for rupture properties based upon 3-D directivity effect and application to deep earthquakes in the Sea of Okhotsk region. *Geophysical Journal International*, *203*(2), 1011–1025. https://doi.org/10.1093/gji/ggv352

Prieto, G. A., Froment, B., Yu, C., Poli, P., & Abercrombie, R. E. (2017). Earthquake rupture below the brittle-ductile transition in continental lithospheric mantle. *Science Advances*, *3*(3), e1602642. https://doi.org/10.1126/sciadv.1602642

Prieto, G. A., Parker, R. L., & Vernon, I. F. L. (2009). A Fortran 90 library for multitaper spectrum analysis. *Computers and Geosciences*, *35*(8), 1701–1710. https://doi.org/10.1016/j.cageo.2008.06.007

Ross, Z. E., & Ben-Zion, Y. (2016). Toward reliable automated estimates of earthquake source properties from body wave spectra. *Journal of Geophysical Research: Solid Earth*, *121*, 4390–4407. https://doi.org/10.1002/2016JB013003

Ross, Z. E., Kanamori, H., & Hauksson, E. (2017). Anomalously large complete stress drop during the 2016 M_w 5.2 Borrego Springs earthquake inferred by waveform modeling and near-source aftershock deficit. *Geophysical Research Letters*, *44*, 5994–6001. https://doi.org/10.1002/2017GL073338

Seekins, L. C., & Boatwright, J. (2010). Rupture directivity of moderate earthquakes in northern California. *Bulletin of the Seismological Society of America*, *100*, 1107–1119. https://doi.org/10.1785/0120090161

Tomic, J., Abercrombie, R. E., & Do Nascimento, A. (2009). Source parameters and rupture velocity of small $M \leq 2.2$ reservoir induced earthquakes. *Geophysical Journal International*, *179*, 1013–1023. https://doi.org/10.1111/j.1365-246X.2009.04233.x

Van Houtte, C., Bannister, S., Holden, C., Bourguignon, S., & McVerry, G. (2017). The New Zealand strong motion database. *Bulletin of the New Zealand Society for Earthquake Engineering*, *50*(1), 1–20.

Waldhauser, F., & Ellsworth, W. L. (2000). A double-difference earthquake location algorithm: Method and application to the northern Hayward fault, California. *Bulletin of the Seismological Society of America*, *90*(6), 1353–1368. https://doi.org/10.1785/0120000006

Wallace, L. M., Bartlow, N., Hamling, I., & Fry, B. (2014). Quake clamps down on slow slip. *Geophysical Research Letters*, *41*, 8840–8846. https://doi.org/10.1002/2014GL062367

Wang, E., Rubin, A. M., & Ampuero, J.-P. (2014). Compound earthquakes on a bimaterial interface and implications for rupture mechanics. *Geophysical Journal International*, *197*(2), 1138–1153. https://doi.org/10.1093/gji/ggu047

Warren, L. M., Baluyut, E. C., Osburg, T., Lisac, K., & Kokkinen, S. (2015). Fault plane orientations of intermediate-depth and deep-focus earthquakes in the Japan-Kuril-Kamchatka subduction zone. *Journal of Geophysical Research: Solid Earth*, *120*, 8366–8382. https://doi.org/10.1002/2015JB012463

Warren, L. M., & Silver, P. G. (2006). Measurement of differential rupture durations as constraints on the source finiteness of deep-focus earthquakes. *Journal of Geophysical Research*, *111*, B06304. https://doi.org/10.1029/2005JB004001

Wessel, P., & Smith, W. H. F. (1998). New, improved version of the Generic Mapping Tools released. *Eos, Transactions, American Geophysical Union*, *79*(47), 579. https://doi.org/10.1029/98EO00426

Williams, C. A., Eberhart-Phillips, D., Bannister, S., Barker, D. H. N., Henrys, S., Reyners, M., & Sutherland, R. (2013). Revised interface geometry for the Hikurangi subduction zone, New Zealand. *Seismological Research Letters*, *84*(6), 1066–1073. https://doi.org/10.1785/0220130035

Yamada, T., Mori, J. J., Ide, S., Kawakata, H., Iio, Y., & Ogasawara, H. (2005). Radiation efficiency and apparent stress of small earthquakes in a South African gold mine. *Journal of Geophysical Research*, *110*, B01305. https://doi.org/10.1029/2004JB003221